The electronic and magnetic structure of bcc iron-nickel alloy

1999 J. Phys.: Condens. Matter 11 1545

(http://iopscience.iop.org/0953-8984/11/6/019)

J. Phys.: Condens. Matter **11** (1999) 1545–1556. Printed in the UK PII: S0953-8984(99)96713-9

The electronic and magnetic structure of bcc iron–nickel alloy

M E Elzain, A A Yousif, A D Al Rawas and A M Gismelseed

Department of Physics, College of Science, Sultan Qaboos University, Box 36, Al Khod 123, Sultanate of Oman

Received 11 August 1998, in final form 27 November 1998

Abstract. The first principles discrete variational method and the local density approximation are used to calculate the electronic and magnetic properties of clusters of iron and nickel atoms representing the bcc iron–nickel alloy with nickel concentration up to about 30%. It is found that the presence of nickel atoms at sites neighbouring iron increases the iron local magnetic moment but decreases the magnitude of the magnetic hyperfine field. The magnetic hyperfine field at the iron site increases with increasing number of nickel atoms at the next-nearest-neighbour sites. Consequently, the experimentally observed maximum in both magnetization and hyperfine field versus nickel concentration is attributed to different iron sites. The 3d local densities of states at iron and nickel sites are calculated. The average density of states is found to remain unaltered for the majority sub-band, whereas it exhibits large deformation for the minority sub-band. An energy diagram is deduced from the density of states and is used to explain the formation of magnetic moment at iron and nickel sites. We deduce the following from these calculations. The observed increase in the local magnetic moment in the iron site is attributed to the reduction in the weight of the bonding d states and the accompanying constancy of the weight of the antibonding states, which ar driven by sd interaction.

1. Introduction

The addition of nickel to iron greatly enhances the strength and corrosion resistance of iron. In its α-phase, the iron–nickel alloy forms the base of structural steel; henceforth, the mechanical properties of these alloys received more attention as compared to other properties. In contrast, more emphasis is placed on the study of the magnetic properties of alloys in the γ-phase. It could be beneficial to use the models developed to explain the magnetic properties in improving our understanding of the mechanical properties, especially where Mössbauer spectroscopy is a common tool in both studies.

The Fe_{1-x} Ni_x alloys, with x less than about 0.3, are body centred cubic solid solutions with a lattice constant close to that of α-iron. Both, the average magnetic moment and the average hyperfine field were found to possess flat maximum at about 20 at.% nickel concentration [1]. On the other hand, the local magnetic moment at the iron site was found to increase with increasing nickel content, whereas the local nickel moment remains almost constant. Similar trends were obtained for mechanically alloyed nano-crystals and ultra-thin films [2].

The electronic and magnetic properties of the α-phase had been studied by Hasegawa and Kanamori [3] using the single site coherent potential approximation (CPA), which was combined with the Hartree–Fock approximation in a tight-binding model. The calculated average moment and density of states at the Fermi level were found to agree with experimental results. In this contribution the local properties at the iron and nickel sites, with various local environments, are calculated. It is found that the local iron moment increases with increasing

0953-8984/99/061545+12$19.50

number of nickel atoms at the nearest-neighbour sites, whereas the nickel moment exhibits little variation. On the other hand, the magnetic hyperfine field at the iron site is found to increase with increasing number of nickel atoms at the next-nearest-neighbouring site. Therefore, the major contributions to the changes in average moment and average magnetic hyperfine field at the iron site arise from different iron sites. The average local majority density of states (DOS) is found to experience negligible deformation as the nickel concentration increases, while the minority DOS is greatly deformed. This is attributed to the difference in the effective energy of the minority sub-bands at the iron and nickel sites. The peaks in the DOS are associated with the bonding and antibonding molecular levels and the resulting energy diagram is used to explain the magnetism of α-iron, bcc nickel and the bcc iron–nickel alloy. Using this energy diagram we deduce the following results. The bonding majority and minority sub-bands in α-iron, bcc nickel and iron–nickel alloy are full and hence do not contribute to the magnetic moment. The observed values of the local magnetic moments could be obtained when a reduction in the number of bonding states is invoked while the number of antibonding states remains constant. It is proposed that the sd interaction is the mechanism leading to this behaviour.

In the following section we briefly outline the method used to perform the calculation of the electronic and magnetic properties. The results are presented and discussed in section 3, whereas a short summary is presented in section 4.

2. Theoretical model

The iron-rich iron–nickel alloy is represented by a set of clusters of iron and nickel atoms, where each cluster consists of the first, second and third neighbouring shells around the central atom. Because, in general, the central atom has a number of its neighbouring shells complete we believe that its description should represent the corresponding properties of the bulk solid better than would those of atoms in the outer co-ordination shells. In the following we use the calculated results at the central sites to draw conclusions on the iron–nickel alloy. Since the electronic and magnetic properties of α-iron are well known, we have selected the cluster configuration, which gives comparable values to the established results. In this respect, we found that a cluster of 19 atoms composed of the first, second and four atoms from the third neighbouring shell give reasonable values that are comparable to values reported in the literature [4].

The local properties at the central site are more sensitive to variations in the types of atom at the first and second co-ordination shells than to the corresponding variations in the further shells. Hence, we study clusters with varying number of nickel atoms at the nearest- and next-nearest-neighbour shells around the central atom. Iron-centred and nickel-centred clusters are denoted by Fe$[N, M]$ and Ni$[N, M]$ respectively. Here N and M are the respective number of nickel atoms at the first and second neighbouring shells. The clusters Fe$[0, 0]$ and Ni$[0, 0]$ respectively represent iron and nickel in α-iron, whereas the clusters Fe$[8, 6]$ and Ni$[8, 6]$ represent iron and nickel in bcc nickel. Under the assumption that the relative locations of atoms within a shell are not important, there are 63 different cluster configurations for each of the iron- and nickel-centred clusters. We have calculated the properties at the central site for 12 out of the 63 cluster configurations. To study the properties of the alloy, we need first to estimate the local properties at the central sites of the remaining configurations. We do this through interpolation. For example if the value of a local property $Q(N, M)$ is calculated for $N = N_1$ and $N = N_2$ for some fixed M then the value of Q for an intermediate N is obtained from the relation $Q(N, M) = Q(N_1, M)+C(N-N_1)^r$. In this relation C is a constant determined from the calculated value of the property for $N = N_2$ and r is a constant determined by comparing the calculated and experimental results. When comparing to experimental results, we found that in some cases the dependence on N is linear and in other it is non-linear as will be seen

later. Secondly, we assume that the probability of realization of a cluster of configuration (N,M) is given by the binomial distribution

$$p(N, M) = x_1^N (1 - x_1)^{8-N} x_2^M (1 - x_2)^{6-M}.$$

The probabilities x_1 and x_2 of the site occupation of the first and second shells are determined by the nickel concentration c through $x_i = c + \beta c(1-c)$, where $i = 1, 2$ and β is a short-range order parameter. For a completely disordered system $\beta = 0$. The average property $\bar{Q}$ is then given by

$$\bar{Q} = \sum_{NM} Q(N, M) p(N, M).$$

We have used the first principles discrete variational method to solve the spin polarized Kohn–Sham equation in the local density approximation employing the von Barth and Hedin exchange–correlation potential [5]. Since the lattice constant in iron–nickel alloy change slightly with nickel concentration, we have chosen to make the calculation at a fixed lattice constant, for which we chose $a = 5.4$ au. The wavefunction is expanded in terms of Fe and Ni valence atomic orbitals, with a frozen core, and the equations are integrated using the diophantine sampling and Gaussian quadrature in different regions of space. The clusters are embedded in a constant potential, which is set at the bottom of the valence energy level, while the valence wavefunctions asymptotically approach plane waves in the region outside the cluster volume [6].

The local magnetic hyperfine field B_{hf} at a central site is calculated using the phenomenological relation presented in [7]. The hyperfine field is split into core and valence terms. The core contribution B_{hfc}, is assumed to be directly proportional to the local 3d moment, μ_d, while the valence contribution is computed directly. Ebert *et al* [8], using the KKR–CPA approximation, calculated the proportionality constant of B_{hfc} to be μ_d, for fcc iron–nickel alloys. Their results gave values varying from about 10 to 12 T μ_B^{-1}.

3. Results and discussions

In table 1 we present the 3d and sp magnetic moments (in Bohr magnetons), the valence contact charge density ρ and the valence contact spin density $\Delta\rho$ (in au) and the magnetic hyperfine field (in teslas), at the central iron site. We note that, indeed, the local magnetic moment increases with increasing nickel content. On the other hand, the magnetic hyperfine field reflects a different trend. Its magnitude decreases when nickel occupies the nearest-neighbouring shell and increases when nickel occupies the next-nearest-neighbouring shell. The contact charge density is seen to decrease with increasing nickel content leading to a

Table 1. The respective local 3d and sp magnetic moments μ_d and μ_{sp} in Bohr magnetons, the respective contact charge and spin densities ρ and $\Delta\rho$ in atomic units and the magnetic hyperfine field B_{hf} in teslas at the central iron site in configurations Fe $[N, M]$, where N and M are the number of nickel atoms at the nearest- and next-nearest-neighbour sites of the central iron atom respectively.

	Fe [0, 0]	Fe [0, 6]	Fe [8, 0]	Fe [8, 6]
μ_d	2.37	2.54	2.71	2.91
μ_{sp}	−0.18	−0.18	−0.03	0.02
ρ	5.81	5.80	5.46	5.46
$\Delta\rho$	−0.11	−0.18	0.10	0.23
B_{hf}	−34	−40	−28	−23

Table 2. The respective local 3d and sp magnetic moments μ_d and μ_{sp} in Bohr magnetons, the contact spin densities $\Delta\rho$ in atomic units and the magnetic hyperfine field B_{hf} in teslas at the central nickel site in configurations Ni $[N, M]$, where N and M are the number of nickel atoms at the nearest- and next-nearest-neighbour sites of the central nickel atom respectively.

	Ni [0, 0]	Ni [0, 6]	Ni [8, 0]	Ni [8, 6]
μ_d	0.67	0.63	0.58	0.51
μ_{sp}	−0.21	−0.15	−0.07	−0.04
$\Delta\rho$	−0.38	−0.51	−0.19	−0.09
B_{hf}	−28	−34	−17	−11

positive isomer shift in agreement with experimental result [1]. The corresponding results for nickel-centred clusters are shown in table 2. The calculated magnetic moment for Ni[0, 0] agrees with that of Anisimov *et al* [9] for nickel in α-iron and the result of the cluster Ni[8, 6] agrees in general with those reported for bcc nickel [10, 11]. We note that the total magnetic moment at the nickel site remains almost constant, whereas the magnitude of the magnetic hyperfine field decreases with increasing number of nickel atoms at the first shell. In addition, the magnitude of B_{hf} at the nickel site increases with increasing number of nickel atoms at the second shell.

3.1. Density of states and exchange splitting

The 3d partial density of states at the central site in iron-centred and nickel-centred clusters exhibits two prominent peaks with a dip in between, typical of the body centred cubic lattices. These two peaks are in general attributed to the bonding and antibonding states [12]. For spin-polarized systems the majority and minority sub-bands are shifted by the exchange splitting. In α-iron the Fermi level is at the minimum of the minority sub-band and near the top of the majority sub-band. Most of the contribution to the density of states at the Fermi level, $n(E_f)$, in α-iron arise from the majority sub-band. On addition of nickel the situation is reversed and the contribution from the minority sub-band dominates with increasing nickel concentration. The dominance of the contribution of the minority sub-band is in agreement with the result of Drittler *et al* [13], who calculated the change in $n(E_f)$ for nickel impurity in α-iron. Furthermore, we found that the average $n(E_f)$ per atom increases with increasing nickel concentration and follows the experimental trends as determined by specific heat measurement [14]. This is depicted in figure 1, where the average $n(E_f)$ is scaled by the corresponding quantity for α-iron and only the 3d contribution is taken into account. To attain agreement between experiment and calculation, we have assumed that the local density of states for Fe$[N, M]$ changes from the calculated value of $N = 0$ to $N = 8$ as the fifth power of N. Similar trends were observed for the magnetic moments below as the figure shown there illustrates.

In figure 2 we plot the average 3d partial density of states versus energy for different nickel concentrations. We note that the basic structure of the majority sub-band is retained as the nickel concentration increases except for a noticeable increase in the weight of the bonding component of states. This enhancement in the density of the bonding states might be the reason behind the strengthening effect that nickel endows on steel. On the other hand, the minority sub-band is observed to experience structural deformation with increasing nickel concentration. The observed patterns are ascribed to the difference in the energy of the atomic levels. The atomic level of nickel is deeper than that of iron. However, the exchange splitting at the iron site is larger than that at the nickel site and it increases with increasing nickel content as shown in figure 3. The exchange splitting between the majority and minority sub-bands $\Delta = E\uparrow - E\downarrow$ is obtained through the calculation of the effective levels $E_\sigma = \int E n_\sigma(E)\,\mathrm{d}E$ at

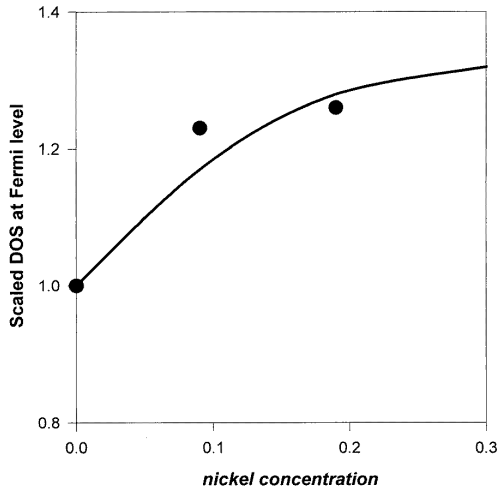

Figure 1. The calculated (continuous line) and measured (full circle) average densities of states at the Fermi level versus the nickel concentration. The densities of states are scaled by the corresponding results for α-iron. Only the 3d contributions are included in the calculated average density of states.

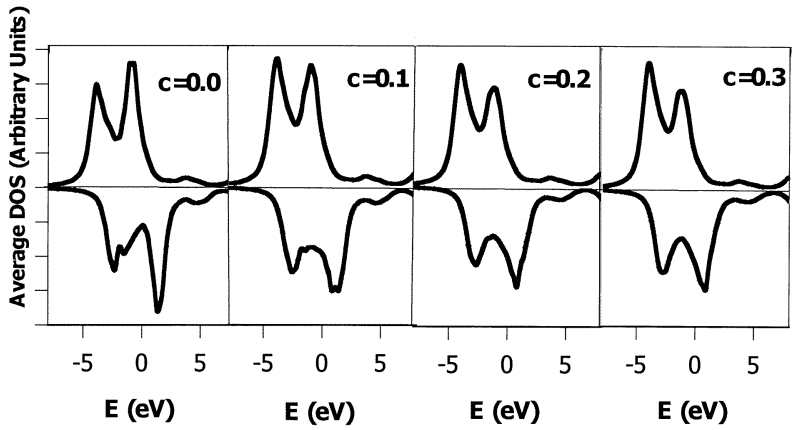

Figure 2. The calculated 3d average densities of state per atom versus energy for different nickel concentrations. Energy is measured from the average Fermi level. The upper curve at each concentration represents the majority sub-band whereas the lower curves represent the minority sub-band.

each site. We found that both the spin-up and spin-down effective levels at the iron site become deeper as nickel concentration increases. On the other hand, the effective levels at the nickel site, which are not far apart, do not change appreciably with increasing nickel concentration. This leads to almost equivalent site energies for the majority sub-bands and very different site energies for the minority sub-bands and consequently to different behaviours of the densities of states. The energy difference between the site energies at iron and nickel in the minority sub-band is large and this may lead to strong disorder among the minority states.

We assume that the bonding and antibonding energy levels formed by the interaction of two atoms are broadened into the 3d bands. The central peak of the lower hump is associated with

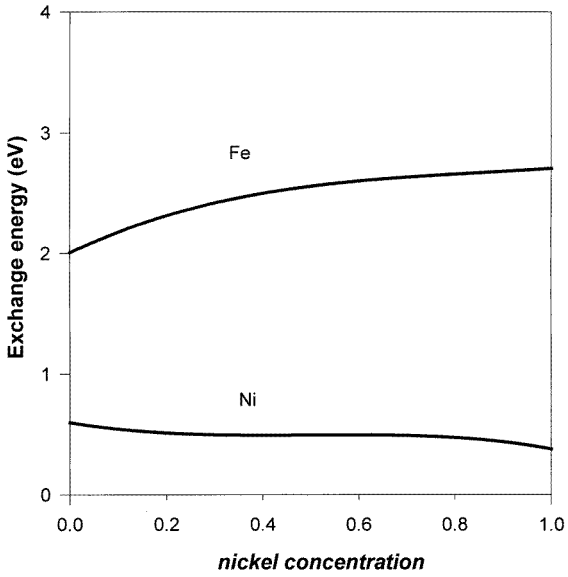

Figure 3. The calculated effective exchange splitting between the majority and minority sub-bands versus nickel concentration. The upper curve is the exchange splitting at the iron site and lower curve is the exchange splitting at the nickel site.

the bonding level, while the peak of the upper hump is associated with the antibonding level. This is a crucial assumption on which rests most of what follows. Under this assumption it is possible to calculate the exchange splitting within the bonding and antibonding bands by determining the energy at the peak of each hump. Within this approach, we found that most of the contributions to the exchange splitting at both iron and nickel sites result from the antibonding states in the nickel rich clusters. For example, we found that the exchange splitting between the bonding states and that between the antibonding states at the iron site in bcc nickel to be about 1.1 eV and 2.1 eV respectively, whereas the same splitting at the iron site in bcc iron is 1.8 eV and 2.3 eV respectively. The exchange splitting resulting from the bonding states at iron sites decreases slightly with increasing nickel concentration, while the corresponding splitting at the nickel site almost vanishes at high nickel concentration. This agrees with the results of Brookes *et al* [11], who measured the exchange splitting at the nickel atom in bcc nickel grown epitaxially on iron, using spin-polarized angle-resolved photoemission. They found that the exchange splitting due to the $\Gamma_{25'}$ states is quite small. These states derive mainly from the coupling between nearest-neighbouring atoms in the bcc structure and constitute most of the occupied bonding states we are referring to [15].

A sketch of the emerging energy picture is shown in figure 4, drawn roughly to scale. The separate atomic energy levels at iron and nickel sites combine to form the bonding and antibonding levels with energies E_b and E_a. The bonding and antibonding energy levels at the iron site in α-iron are split by the exchange splitting as shown in figure 4(a). On addition of nickel, the spin-polarized bonding and antibonding levels are lowered in energy relative to the corresponding levels in α-iron as shown in figure 4(b), where the energy levels at the iron site in bcc nickel are shown. On the other hand, the bonding level at the nickel site in bcc nickel shows no exchange splitting, while the antibonding level is split as shown in figure 4(d). The bonding and antibonding states at the nickel site in α-iron exhibit almost equal exchange splitting as illustrated in figure 4(c). Comparison of the iron levels in nickel and the nickel

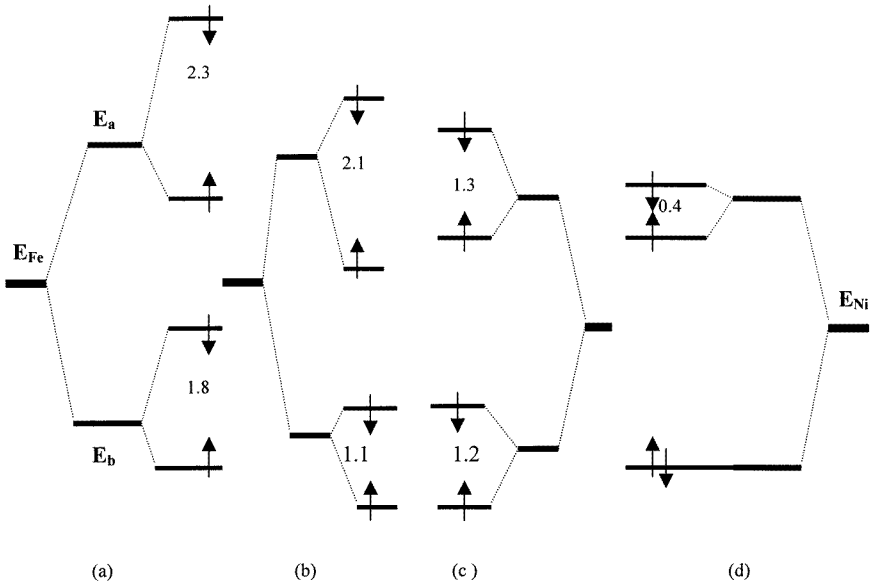

Figure 4. The energy diagram deduced from the calculated densities of states. The atomic level (with energy E_{Fe} or E_{Ni}) splits into bonding and antibonding levels with energies E_b and E_a respectively. The bonding and antibonding levels are each split into majority and minority sub-bands. The numbers show our estimates for the exchange splittings at iron and nickel sites. Part (a) shows the energy for the iron atom in iron, part (b) shows the iron atom in nickel, part (c) shows the nickel atom in iron and part (d) shows the nickel atom in nickel.

levels in nickel (figures 4(b) and (d)) shows that the majority bonding level at the iron site goes below the corresponding nickel level. This may lead to stronger binding and in turn to the strengthening effect of nickel on iron.

3.2. Magnetic moments and hyperfine fields

As the energy diagram in figure 4 shows, the bonding states, which are deep in energy, are expected to contribute little to the local magnetic moment at both sites. We consider here the formation of the magnetic moment at the iron and nickel sites. Let us suppose that the five d states per atom are available to take part in the d–d bonding process. In the case of pure α-iron, which has seven d electrons, five electrons occupy the bonding majority and minority spin sub-bands yielding a zero net magnetic moment. The maximum obtainable magnetic moment is then 2.0 μ_B, resulting from the remaining two electrons residing at the antibonding majority sub-band. This is less than the α-iron moment. A possible conjecture is to assume that the bonding states are not completely full and they contribute positively to the magnetic moment. For pure nickel, which has nine d electrons, five electrons fill the bonding states and the remaining four electrons are shared between the antibonding sub-bands. If the majority antibonding sub-band is filled first, then a net magnetic moment of 1.0 μ_B results, which is higher than the bcc nickel moment. To obtain a reasonable moment in this case, either we assume that the contribution of the bonding states to the magnetic moment is negative, which is unreasonable, or that the majority sub-band in the antibonding states is not full. However, an alternative solution to both cases of iron and nickel moments is possible. This is achieved through the sd interaction which reduces the number of d states at both iron and nickel sites

[16, 17]. We propose that the reduction in the number of d states occurs specifically among the bonding states, while the antibonding states remain almost unchanged.

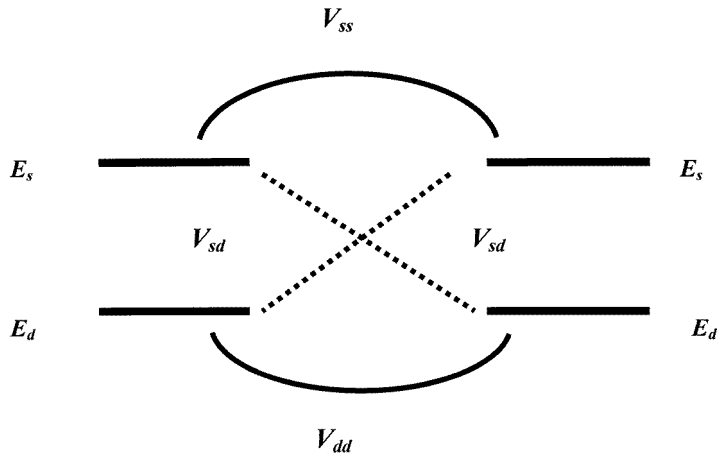

Figure 5. Two identical atoms with two non-degenerate energy levels denoted by E_s and E_d. The two atoms couple through the ss interaction V_{ss}, the dd interaction V_{dd} and the sd interaction V_{sd}.

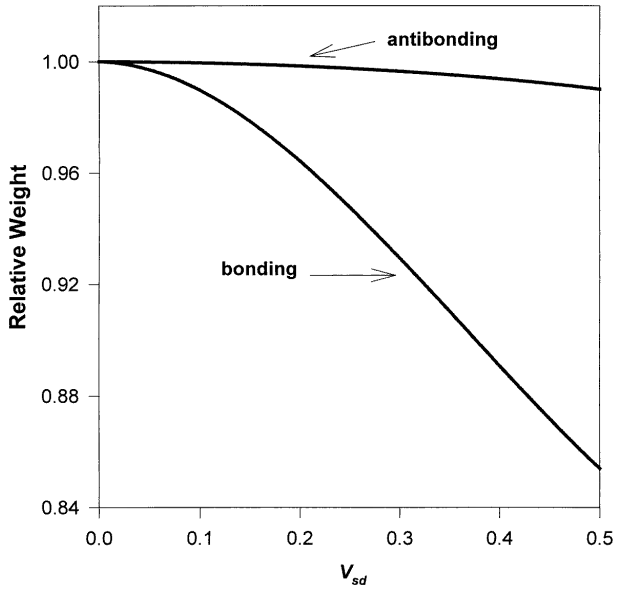

Figure 6. The weight of the d bonding (lower curve) and antibonding (upper curve) for a two atom system versus the sd interaction V_{sd}. The sd interaction V_{sd} is measured in units of V_{dd}. The weights are scaled by the weight for the states with $V_{sd} = 0$.

As an illustration of this conjecture, we consider a simplified model of two atoms, each having two states as shown in figure 5. We denote the atomic energies at each site by E_s and E_d, while the s–s, d–d and s–d couplings are denoted by V_{ss}, V_{dd} and V_{sd} respectively. The Hamiltonian matrix describing the system, in the space of the orthonormal atomic orbitals, is

given by

$$H = \begin{pmatrix} E_d & 0 & V_{dd} & V_{sd} \\ 0 & E_s & V_{sd} & V_{ss} \\ V_{dd} & V_{sd} & E_d & 0 \\ V_{sd} & V_{ss} & 0 & E_s \end{pmatrix}.$$

The s–s and d–d couplings are measures of the respective bandwidths, which result when a solid is formed from a collection of similar atoms. In 3d metals V_{ss} is considerably larger than V_{dd}. We express the energies in units of V_{dd}. As an example, we take V_{ss} equal to four times V_{dd} and $E_s - E_d$ twice V_{dd} and diagonalize H to obtain the eigenvalues and eigenfunctions as functions of V_{sd}. The weight of an atomic orbital in the eigenfunction is taken as the square of the corresponding expansion coefficient. The weights of the d orbitals in the bonding and antibonding states as a function of V_{sd} are shown in figure 6. These weights are scaled by the weights of the corresponding orbitals for $V_{sd} = 0$. It is clear that the weight of the bonding states decreases with increasing V_{sd} while the weight of the antibonding states shows little change. This conclusion is true for all cases when the d band lies in the lower half of the s band. On the hand, when the d band lies in the upper half of the s band, the bonding states will have constant weight, while the weight of the antibonding state decreases. Furthermore, when the d band is at the centre of the s band both states are affected equally. We extended the above Hamiltonian to investigate the effect of d degeneracy on the above conclusions. In a cubic environment the d states split into e_g and t_{2g} components, which have different spatial orientations. The extended Hamiltonian represents states with e_g and t_{2g} symmetry. We found that the same conclusions as regards the decrease in the weight of the totality of the bonding states and the accompanying constancy of the weight of the antibonding states as a function of the sd coupling holds. When looking at variations among the individual bonding states, we found that the decrease among the the low lying bonding state is more than the following bonding state.

Consequently we assume that the sd interaction in iron and nickel reduces the number of d bonding states while keeping the antibonding states unaltered. Furthermore, the total numbers of d electrons are taken to be constant. Hence, reduction in the number of bonding states leads to an increase in the number of antibonding electrons. For example in the case of iron if there are 4.6 electrons filling the bonding states then a magnetic moment of 2.4 μ_B is obtained when the remaining 2.4 electrons are in the antibonding majority sub-band. Similarly a magnetic moment of 0.5 μ_B can be deduced for bcc nickel when some of the excess electrons enter the antibonding minority sub-band.

The main reason behind the increase in the magnetic moment at iron site induced by addition of nickel is the change in weight of the d states at iron and nickel sites [3]. Since the d level at nickel is lower than that at iron, then the weight of the bonding state at the nickel site is higher than its weight at the iron site, whereas the opposite occurs for the antibonding states. This means that more of the bonding electrons reside at nickel and more of the antibonding electrons reside at iron sites. This exchange of electrons between iron and nickel should occur in such a way to keep the two atoms neutral since there is no observed charge transfer. Because the bonding states are full no magnetic moment is induced; however, the addition of electrons to the antibonding majority sub-band at iron site will produce additional magnetic moment.

To relate the calculated magnetic moments and hyperfine fields to the experimental results, we compute the average corresponding quantities for bcc iron–nickel alloy. We take the averages over the two shells of neighbours surrounding the central atom as explained in section 2. Figure 7 shows that the calculated average magnetic moment follows the experimental trend [18], where it initially rises and then decreases with increasing nickel concentration. Note that both the calculated and experimental moments are scaled by the

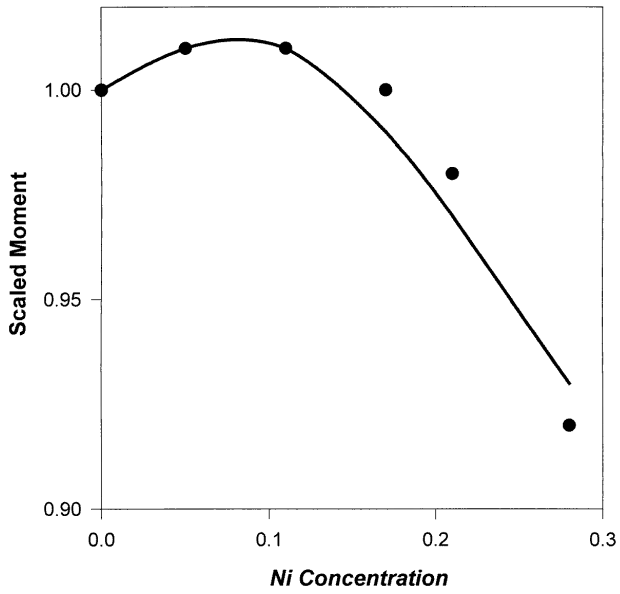

Figure 7. The average magnetic moments per atom versus nickel concentration. The continuous curve represents the calculated average magnetic moment whereas the full circles represent the experimental results of [18]. The average moments are scaled by the corresponding α-iron moments.

corresponding α-iron moment and the alloy is taken as completely disordered (no short-range order). The observed trends in the magnetic moment are reproduced under the assumption that the dependence of the iron local moment on N is non-linear, varying the fifth power of N. Figure 8 shows the dependence of the local iron moment against N for nickel concentration equal to 0.1. The local moment rises sharply with increasing N and saturates for N equal to about 4.

The local magnetic hyperfine field B_{hf} at the iron site decreases in magnitude when nickel atoms are at the nearest-neighbour sites and increases if nickel is at the next-neighbour sites. This is mainly due to sd exchange interaction. A nickel atom at a neighbouring site has a small magnetic moment, which would mean a small sd exchange interaction. On the other hand, a nickel atom at the next-nearest-neighbour site increases the magnetic moment of the iron atoms at the neighbouring sites and consequently the sd exchange interaction between the two neighbouring iron atoms increases. The sd exchange interaction is anti-ferromagnetic and it leads to a negative contact valence spin density at the central site [7]. This spin density is proportional to magnetic moment of the surrounding atoms. We scale the average magnetic hyperfine fields at iron and nickel sites by the corresponding α-iron and bcc nickel hyperfine fields. Figure 9 shows the scaled hyperfine fields versus nickel concentration for the random alloy, where the correct experimental trends are fairly well reproduced [19]. A linear dependence of B_{hf} on N is used. Although the local B_{hf} at the iron site is reduced when a nickel atom occupies a neighbouring site, this is overcompensated by the increase resulting from the occupation by a nickel atom of a next-neighbouring site. The net result is the development of a weak maximum in B_{hf} as nickel concentration increases. Moreover, we have calculated the distribution of the hyperfine fields at the iron site and obtained sharply peaked distributions, which shift to higher values as nickel concentration increases.

From the above observation we conclude that a nickel atom dissolved in iron induces

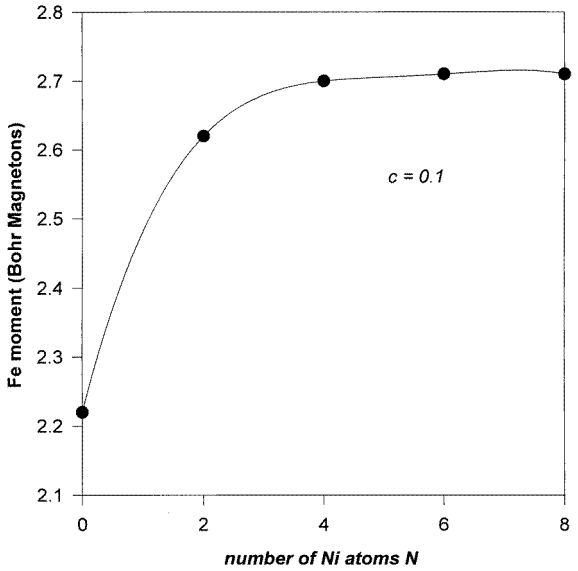

Figure 8. A typical dependence of the local magnetic moment at the iron site against the number of nickel atoms in the neighbouring shell, N for $c = 0.1$. Similar trends are used for other nickel concentrations in order to reach agreement with experimental results.

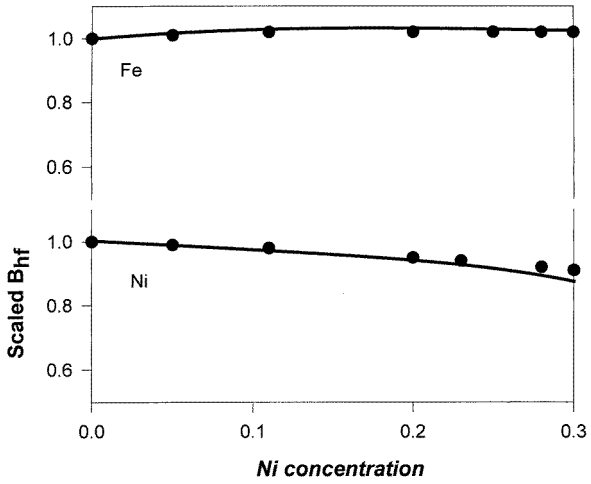

Figure 9. The average magnetic hyperfine fields B_{hf} at iron (upper part) and at nickel (lower part) sites. The continuous curves are the calculated hyperfine fields, while the full circles are the experimental results from [1] (for iron) and [19] (for nickel). The hyperfine fields are scaled by the corresponding α-iron and bcc nickel values.

changes in the properties of iron as follows. The iron atoms in the immediate neighbourhood of nickel have larger magnetic moment, lower charge density and lower hyperfine field as compared to α-iron. The iron atoms, which are next neighbours to nickel, have larger hyperfine field, negligible isomer shift and slightly increased magnetic moment. Consequently the iron sites, which exhibit large hyperfine field, are different from those which show a large local magnetic moment.

4. Summary

The electronic and magnetic structures of bcc iron–nickel alloy were calculated using the local density functional approximation and the first principles discrete variational method. The iron–nickel alloy was represented by a set of clusters of iron and nickel atoms. The 3d local density of states exhibits two peaks, which were assumed to originate from the corresponding bonding and antibonding levels. Using a non-linear dependence of the DOS at the iron site on N, we found that the density of states at the Fermi level, which derives mainly from the minority sub-band, increases with increasing nickel concentration in agreement with experimental findings. An energy diagram is deduced and used to explain the formation of magnetic moment in α-iron, bcc nickel and bcc iron–nickel alloy. It was proposed that the sd interaction reduces the number of d bonding states while it does not change the number of antibonding states. This eventually led to reasonable values for the local magnetic moments at iron and nickel sites and to the explanation of the observed increase in iron magnetic moment with increasing nickel content. The average magnetic moment and hyperfine fields were computed and compared to experimental results. It was found that for average magnetic moment to agree with experimental data, a non-linear dependence of the iron local moment on the number of nickel atoms at neighbouring sites has to be assumed. On the other hand, experimental results for hyperfine fields were reproduced with a linear dependence.

References

[1] Johnson C E, Ridout M S and Cranshaw T E 1963 *Proc. Phys. Soc.* **81** 1079
[2] Kuhrt C and Schultz L 1992 *J. Appl. Phys.* **73** 1975
Faldum T, Meisel W and Gütlich P 1996 *ICAME-95 Conf. Proc.* vol 50, ed I Ortalli (Bologna: SIF) p 615
[3] Hasegawa H and Kanamori J 1972 *J. Phys. Soc. Japan* **33** 1607
[4] Callaway J and Wang C S 1977 *Phys. Rev.* B **16** 2095
[5] Averil F W and Ellis D E 1973 *J. Chem. Phys.* **59** 6412
[6] Lindgren B and Ellis D E 1982 *Phys. Rev.* B **26** 636
[7] Elzain M E, Ellis D E and Guenzberger D 1986 *Phys. Rev.* B **34** 1430
[8] Ebert H, Winter H, Gyroffy B L, Johnson D D and Pinski F J 1988 *J. Phys. F: Met. Phys.* **18** 719
[9] Anisimov V I, Antropov V P, Liechtenstein A L, Gubanov V A and Postnikov A V 1988 *Phys. Rev.* B **37** 5598
[10] Kamada Y, Matsui M and Asada T 1996 *J. Phys. Soc. Japan* **66** 466
Bland J A C Bateson R D, Johnson A D, Heinrich B, Celinski Z and Lauter H J 1991 *J. Magn. Magn. Mater.* **93** 331
Moruzzi V L and Marcus P M 1988 *Phys. Rev.* B **38** 1613
[11] Brookes N B, Clarke A and Johnson P D 1992 *Phys. Rev.* B **46** 237
[12] Mattis D C 1981 *Theory of Magnetism* (Berlin: Springer) p 214
[13] Drittler B, Stefanou N, Blugel S, Zeller R and Dederichs O H 1989 *Phys. Rev.* B **40** 8203
[14] Cheng C H, Wei C T and Beck P A 1960 *Phys. Rev.* **120** 426
[15] Morinaga M, Yukawa N and Adachi H 1985 *J. Phys. F: Met. Phys.* **15** 1071
[16] Kanamori J 1990 *Prog. Theor. Phys. Suppl.* **101** 1
[17] Akai H 1982 *J. Phys. Soc. Japan* **51** 468
[18] Bozorth R M 1993 *Ferromagnetism* (New York: IEEE) p 111
[19] Erich U 1967 *Z. Phys.* **227** 25